Progress on Transonic Flutter and Shock Buffet Computations in Support of the Third Aeroelastic Prediction Workshop

Pawel Chwalowski[*] Bret K. Stanford[†] Steven J. Massey[‡]
Garrett R. McHugh[§] Kevin E. Jacobson[¶]

NASA Langley Research Center, Hampton, VA 23681-2199

This paper reports on the progress of the NASA Langley team contributions to the third Aeroelastic Prediction Workshop's (AePW-3) High Angle Working Group (HAWG). The primary objectives of HAWG is to predict the fluter dynamic pressure of the NASA Benchmark Supercritical Wing (BSCW) configuration at Mach 0.8 and 5° angle of attack. The secondary objective is to determine if a shock-buffet onset is present at or near that flow condition. The computational results are obtained using FUN3D, an unstructured grid Reynolds-averaged Navier-Stokes solver developed at the NASA Langley Research Center. The preliminary analysis results show a computationally-obtained flutter dynamic pressure of approximately 120 psf. Initial results describing unforced BSCW unsteady flow environment at flutter condition are also presented.

I. Introduction

The third AIAA Aeroelastic Prediction Workshop (AePW-3)[a] will take place in conjunction with the AIAA SciTech 2023 conference. In preparation for the workshop, the computational aeroelasticity community decided to split into four working groups: the Large Deflection Working Group (LDWG), the Flight Test Working Group (FTWG), the High Speed Working Group (HSWG), and the High Angle Working Group (HAWG). The LDWG focuses on analysis of the coupled aeroelastic problems associated with large deflections of a relatively flexible, high-aspect ratio wing subjected to low-speed aerodynamics. The FTWG focuses on the body-freedom flutter analysis of NASA's experimental flight vehicle X-56A. The HSWG focuses on fluid-structure-interaction analysis at supersonic to hypersonic speeds, and the HAWG concentrates on transonic flutter and shock buffet computations. Specifically, the HAWG community is challenged to analyze the NASA Benchmark Supercritical Wing (BSCW) configuration and to provide predictions for two cases: (1) flutter dynamic pressure at Mach 0.8 and 5° angle of attack, and (2) unsteady flow and the shock-buffet environment at or near Mach 0.8. These cases build on the computational aeroelastic results generated for the AePW-2 that took place in 2016.[1]

The BSCW was first tested in the NASA Langley Transonic Dynamics Tunnel (TDT) in 1991.[2,3] For this test, the wing was mounted on the TDT Pitch And Plunge Apparatus (PAPA) to obtain the flutter boundary at various Mach numbers and angles of attack for a two-degree of freedom (pitch and plunge) system. In 2000,[4,5] the wing was tested again, this time on a TDT mounting mechanism called the Oscillating Turntable (OTT). The purpose of the OTT tests was to measure aerodynamic response during sinusoidal (forced) pitch oscillation of the wing. The experimental data indicated that the BSCW exhibited a strong shock and separated flow at a moderate angle of attack at transonic conditions. The computations of the transonic flow, in conjunction with the flutter boundary predictions, were the focus of the second workshop.[6] The OTT test also provided some experimental data for the computational analysis of the shock-buffet environment. Specifically, before each forced oscillation test, the wing was set at a fixed angle of attack, and the unsteady pressure data were collected.

This paper reports on the progress of the NASA Langley team's contributions to the HAWG BSCW analysis and builds on the computational aeroelastic results[7] generated for the AePW-2 BSCW configuration using the NASA-Langley-developed computational fluid dynamics (CFD) software FUN3D.[8] The previous publication[7] that summarized the computational results generated for the AePW-2 workshop included discussion on the numerical flutter

[*]Senior Aerospace Engineer, Aeroelasticity Branch, Senior Member AIAA.
[†]Research Aerospace Engineer, Aeroelasticity Branch, AIAA Associate Fellow.
[‡]Research Aerospace Engineer, Aeroelasticity Branch, AIAA Member.
[§]Research Aerospace Engineer, Aeroelasticity Branch, AIAA Member.
[¶]Research Aerospace Engineer, Aeroelasticity Branch, AIAA Member.
[a]https://nescacademy.nasa.gov/workshops/AePW3/public/

boundary prediction due to the influences of: (1) temporal and spatial resolution, (2) the coupling scheme between the flow and the structural solvers, and (3) the initial excitation conditions at the two transonic conditions. This paper draws from these experiences and also extends the previous methods from the classical time-domain flutter computations to the linearized frequency-domain analysis.[9] The numerical results at Mach 0.8 are compared to the limited experimental data obtained during the PAPA test and are expanded to additional angles of attack. In addition, preliminary comparisons of the raw OTT experimental and computational surface pressure data at Mach 0.8 are presented. Some Fast Fourier Transform (FFT) of pressure coefficient time histories are also computed and presented.

II. BSCW Model and Test Cases

The BSCW model, shown in Figure 1, has a simple, rectangular, 16- x 32-inch wing planform, with a NASA SC(2)-0414 airfoil. For both the PAPA and OTT tests, the model was mounted to a large splitter plate, sufficiently offset from the wind-tunnel wall (40 inches) to (1) place the wing closer to the tunnel centerline and (2) be outside the tunnel wall boundary layer.[10] The wing was designed to be rigid, with the following structural frequencies for the combined installed wing and OTT mounting system: 24.1 Hz (spanwise first bending mode), 27.0 Hz (in-plane first bending mode), and 79.9 Hz (first torsion mode). When installed on the PAPA mount, the combined system frequencies were 3.33 Hz for the plunge mode and 5.20 Hz for the pitch mode. For instrumentation, the model had pressure ports at two chordwise rows at the 60% and 95% span locations, with 22 ports on the upper surface, 17 ports on the lower surface, and 1 port at the leading edge for each row. The BSCW/PAPA data consists of unsteady data at flutter points and averaged data on a rigidified apparatus at the flutter conditions. For this PAPA test, both the inboard row of pressures at the 60% span station and the outboard row at the 95% span station were populated with unsteady in situ pressure transducers. For the OTT test, however, only the inboard row at the 60% span station was populated with unsteady in situ pressure transducers.

The BSCW test case used in AePW-1 was Mach 0.85 and 5° angle of attack. This proved to be more challenging than expected due to the shock-induced separated flow that dominated the upper surface and the aft portion of the lower surface at that condition. Using this information as a guide, two test cases just outside the separated flow regime were emphasized for AePW-2. These are listed in Table 1. Steady and forced oscillation analyses were conducted at Mach 0.7 and 3° angle of attack, and flutter analyses were conducted at Mach 0.74 and 0° angle of attack. An optional Case #3 at Mach 0.85 and 5° angle of attack, which was the reanalysis of the AePW-1 case, was also prepared, and the participants were encouraged to apply higher fidelity tools. As shown in Table 1, this optional case was divided into three separate subcases based on the type of dynamic data acquired: unforced unsteady, forced oscillation, and flutter.

Based on additional analyses of the experimental data by Heeg and Piatak,[5] it was concluded that the Mach 0.8 and 5° angle of attack condition is a challenging one for flutter analysis using computational aeroelastic software. The flutter event is most likely bounded by the mixed attached and separated flow, and it is hypothesized that the buffeting flow contributes to the flutter onset. Therefore, with the OTT and PAPA experimental data available, this BSCW flow condition was selected for the topic of the third workshop as a natural extension to AePW-1 and AePW-2. These AePW-3 test cases are listed in Table 2. Detailed flow conditions across the range of dynamic pressures were generated using the TDT tunnel parameter code and are shown in Table 3. It is important to note that NASA has plans to retest BSCW on the PAPA in the TDT in year 2023 and to utilize modern optical experimental methods, with the hope of providing additional experimental data for computational aeroelasticity software validation.

Table 1. AePW-2 Workshop Test Cases.

	Case #1	Case #2	Optional Case #3a	Optional Case #3b	Optional Case #3c
Mach	0.7	0.74	0.85	0.85	0.85
AoA	3°	0°	5°	5°	5°
Dynamic Data Type	Forced Oscillation f = 10Hz, $\|\theta\|$=1°	Flutter	Unforced Unsteady	Forced Oscillation f = 10Hz, $\|\theta\|$=1°	Flutter
Notes	- Attached flow - OTT exp. data - R-134a	- Flow state unknown - PAPA exp. data - R-12	- Separated flow - OTT exp. data - R-134a	- Separated flow - OTT exp. data - R-134a	- Separated flow - No exp. data - R-134a

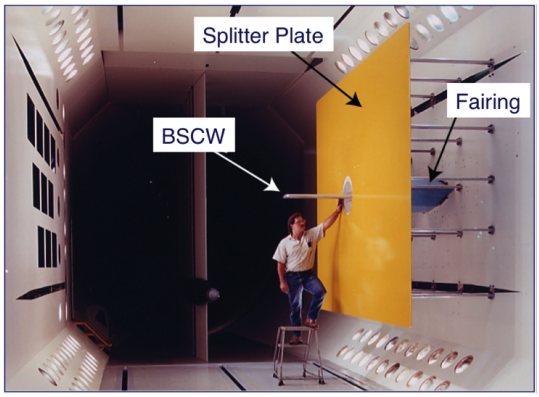

(a) Photograph of the BSCW model mounted on the OTT in the TDT.

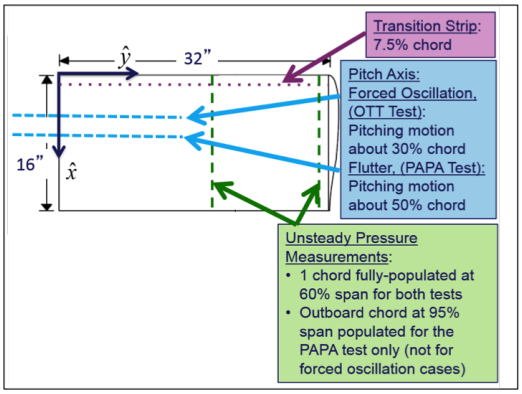

(b) BSCW geometry.

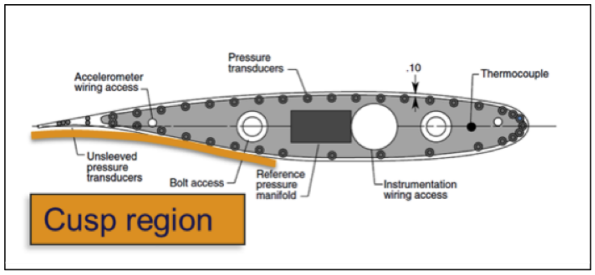

(c) Cross-sectional view of the SC(2)-0414 airfoil, with BSCW instrumentation.

Figure 1. BSCW Model.

Table 2. AePW-3 Workshop Test Cases.

	Case #1	Case #2
Mach	0.8	0.8
AoA	5°	5°
Dynamic Data Type	Flutter Unsteady	Unforced Unsteady
Notes	- Attached / Separated - PAPA exp. data - R-134a	- Shock buffet (?) - OTT exp. data - R-134a

Table 3. BSCW Flow Conditions: Mach 0.8 with range of dynamic pressure (q); chord Reynolds number (Re_c); Reynolds number per foot (Re); velocity (V); speed of sound (a); static temperature, (T_{static}); density (ρ); ratio of specific heat (γ); viscosity (μ); Prandtl number (Pr); total pressure (H); and static pressure (P).

Mach	0.799	0.8	0.8	0.8	0.8	0.8	0.8	0.8	0.8	0.8	0.8	0.801	0.801
q [psf]	10.02	25.00	35.00	50.00	75.00	100.00	134.00	143.00	152.00	168.80	200.00	225.00	250.00
Re_c	237461	592224	829213	1184801	1777732	2371336	3178880	3392751	3606668	4006103	4748658	5343835	5939368
Re [1/ft]	178096	444168	621910	888601	1333299	1778502	2384160	2544563	2705001	3004577	3561493	4007876	4454526
V [ft/s]	440.45	440.63	440.59	440.51	440.39	440.21	440.05	440.00	439.96	439.88	439.70	439.58	439.46
a [ft/s]	551.08	550.94	550.85	550.71	550.48	550.25	549.94	549.86	549.78	549.62	549.34	549.11	548.88
T_{static} [$^\circ F$]	80.87	80.83	80.83	80.82	80.81	80.80	80.78	80.77	80.77	80.76	80.74	80.73	80.71
ρ [slug/ft^3]	0.000103	0.000258	0.000361	0.000515	0.000774	0.001032	0.001384	0.001477	0.001571	0.001745	0.002069	0.002329	0.002589
γ	1.1121	1.1122	1.1123	1.1124	1.1126	1.1128	1.1131	1.1131	1.1132	1.1133	1.1136	1.1138	1.1139
μ [lb-sec/ft^2]	2.555e-07	2.555e-07	2.555e-07	2.555e-07	2.555e-07	2.555e-07	2.554e-07	2.554e-07	2.554e-07	2.554e-07	2.554e-07	2.554e-07	2.554e-07
Pr	0.68394	0.68404	0.68410	0.68419	0.68435	0.68450	0.68471	0.68477	0.68483	0.68493	0.68513	0.68528	0.68544
H [psf]	40.00	99.72	139.61	199.45	299.18	399.00	534.69	570.61	606.53	673.59	798.21	898.01	997.83
P [psf]	28.21	70.32	98.45	140.64	210.97	281.37	377.05	402.38	427.71	475.00	562.87	633.25	703.64

III. Numerical Method

A. Grids

For this preliminary flutter study, unstructured grids consisting primarily of tetrahedra and prisms that were previously prepared for the first two workshops were used. These grids were generated using VGRID[11] with input prepared using GridTool.[12] The tetrahedral elements within the boundary layer were converted into prism elements using preprocessing options within the FUN3D software. Based on the AePW gridding guidelines,[13] three grids belonging to the same family were then constructed: one with 3 million nodes, one with 9 million nodes, and one with 27 million nodes. These grids and the corresponding FUN3D solutions are referred to as 'coarse', 'medium' and 'fine', respectively. In this paper, only the coarse and fine grids were used to generate FUN3D flutter results. The resulting two grid distributions for both the surface and the plane of symmetry are presented in Figure 2.

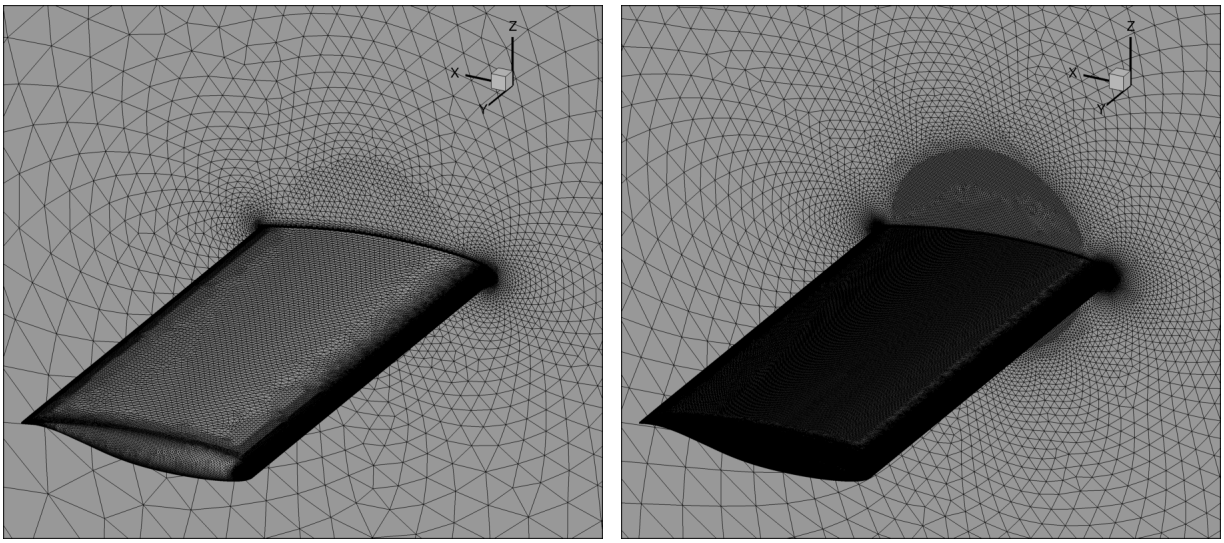

(a) Coarse Grid, 3 Million Nodes.

(b) Fine Grid, 27 Million Nodes.

Figure 2. Coarse and Fine Grids.

B. Rigid Steady Flow Analysis - FUN3D

Solutions to the Reynolds-averaged Navier-Stokes (RANS) equations were computed using the FUN3D flow solver with turbulence closure obtained using the "standard" Spalart-Allmaras (SA) one-equation model.[14,15] The flux limitation was accomplished with the Venkatakrishnan[16] limiter, and inviscid fluxes were computed using the Roe scheme.[17]

For the asymptotically-steady cases, time integration was accomplished by an Euler implicit backwards difference scheme, with local time stepping to accelerate convergence. Most of the cases in this study were run for about 5,000 iterations to achieve convergence. However, some oscillation of forces and moments at transonic conditions is noted, indicating shock motion and separated flow.

C. Time-Domain Dynamic Analysis - FUN3D

Dynamic analyses of the BSCW configuration requires unsteady-flow analysis. For unsteady-flow analysis, the FUN3D solver utilizes the dual-time-stepping method, which is widely used in CFD. This method involves adding a pseudo-time derivative of the conserved variables to the physical time derivative that appears in the time-dependent Navier-Stokes equations, in much the same way that an artificial time term is often added to the steady Navier-Stokes equations to facilitate an iterative solution to a steady state. In the same way as for steady state, as long as the pseudo-time derivative vanishes as the iterations proceed within each time step, at the end of the iterative process, a solution to the original unsteady Navier-Stokes equations is obtained for that physical time step. Iteratively advancing each time step in pseudo-time allows errors introduced by the (generally inexact) linearization of the nonlinear residual to be reduced to zero, assuming the iterations in pseudo-time are fully converged. An additional advantage of the pseudo-time term is that it enhances the diagonal dominance of the linear system, increasing robustness and allowing larger physical time steps to be taken than might otherwise be possible. For an infinitely large physical time step, the dual-time solver becomes identical to the steady-state solver, though of course, all time accuracy is lost.

Aeroelastic analysis with body-fitted meshes requires a grid deformation capability. The grid deformation in FUN3D is treated as a linear elasticity problem.[18] In this approach, the grid points near the body can move significantly, while the points farther away may not move much. In addition to the moving body capability, the analysis of the BSCW configuration requires a structural dynamics capability. For a dynamic aeroelastic analysis, FUN3D is capable of being loosely coupled with an external finite element solver,[19] or in the case of the linear structural dynamics used in this study, an internal modal structural solver can be utilized.[18] This modal solver is formulated and implemented in FUN3D in a manner similar to other NASA Langley aeroelastic codes (CAP-TSD[20] and CFL3D[21]). For the BSCW computations presented here, the structural modes were obtained via a normal modes analysis (solution 103) with the Finite Element Model (FEM) solver MSC Nastran^{TM}.[22] The modes were then interpolated to the surface mesh using the method developed by Samareh.[23] The BSCW FEM was built by Heeg and described in Ref. 24. There are two methods implemented in FUN3D for temporal integration of the structural solver. These methods are the Predictor-Corrector (P-C) scheme and the Backward-Difference (BDF) scheme.[7]

The BSCW dynamic analysis was performed in a multistep process. First, the steady CFD solution was obtained on the rigid body. In the case of a dynamic aeroelastic flutter solution, a static aeroelastic solution was then obtained by restarting the CFD analysis from the rigid-steady solution in a time-accurate mode[25] with a structural modal solver, allowing the grid to deform. A high value of structural damping ratio (0.9999) was used so the structure could find its equilibrium position with respect to the mean flow before the dynamic response was started. Finally, the flutter solution was restarted from the static aeroelastic solution by setting the structural damping value to zero and providing an initial excitation 'kick' in the form of the generalized velocity. The effects of that initial excitation on the flutter solution are described later in this paper.

D. Linearized Frequency-Domain with Mesh Adaptation Analysis - FUN3D

Flutter solutions via the unsteady RANS (uRANS) equations described in the previous section are most commonly obtained with time-integration, but an alternative workflow is the Linearized Frequency-Domain (LFD) method. This scheme, which has recently been implemented[9] around a stabilized finite element (SFE) solver[26] embedded within the FUN3D software, involves infinitesimal oscillatory perturbations about a converged steady-state flow solution. A complex-valued linear system of equations is computed for each mode shape (oscillatory surface motion input) and frequency of interest; the resulting complex-valued oscillatory flow fields can be used to calculate a set of generalized aerodynamic forces (GAFs). These GAFs are identical in form to those output from a "classical" linear aeroelastic analysis built on the doublet lattice method (DLM), and they may be used to directly solve for the flutter-q via a $p-k$ eigen-analysis.

The LFD results shown in this paper have been computed within a mesh adaptation workflow that is summarized in Ref. 27, with mesh adaptation mechanics handled via *refine*[b]. The adaptations reduce spatial interpolation error in the flow field based on some scalar field, which for this work is Mach number. For unsteady simulations, the fixed-point

[b]Available via https://github.com/NASA/refine, last accessed June, 2021.

multiscale metric[28] is computed as an average of the Mach interpolation error tensor sampled at regular intervals of the unsteady simulation. For LFD, flow snapshots are constructed using a harmonic perturbation.

The LFD-based mesh adaptation proceeds as follows:

1. For a given AoA and a given BSCW mesh, the FUN3D/SFE tool is used to compute the steady flow around the wing.
2. The LFD equations are solved across a range of frequencies, for both pitch and plunge perturbations. The resulting GAFs are then processed through a $p-k$ solver to compute the flutter-q.
3. Using the pitch/plunge flutter eigenmode, the complex-valued flutter flow field is computed. A time history of oscillatory snapshots is then constructed via a perturbation expansion: $M = M_0 + real(\delta \cdot \overline{M} \cdot e^{i \cdot \omega \cdot t})$, where M_0 is the steady Mach number field and $\overline{M}$ is the complex-valued flutter flow field. This step also requires the selection of a perturbation level δ and the number of snapshots across a single oscillation.
4. With these snapshots, *refine* constructs the multiscale metric and then creates a new mesh with its adaptation mechanics.
5. The steady pitching moment about the elastic axis (which is the midchord for the BSCW), the flutter dynamic pressure, and the pitch stiffness are used to compute the rotation needed to bring the system into pitch equilibrium. The AoA is updated as the sum of the fixed (set) AoA and this pitch rotation.
6. The process repeats back to step 1, with the new mesh and the new AoA.

The last two steps in the above process represent a loosely-coupled approach to static aeroelasticity, where the static aeroelastic pitch rotation converges alongside the mesh refinement process.

IV. AePW-3 Test Case #1

The first AePW-3 test case involves BSCW flutter prediction at Mach 0.8 and 5° angle of attack. As described previously, for the time-domain analysis, the rigid steady solution is obtained first, followed by the static aeroelastic solution. The third step is to perform dynamic aeroelastic FUN3D computations. The wing response in the form of the time-varying pitch angle is then computed and used to calculate the damping ratio using the matrix-pencil method.[29] For a stable solution, the damping ratio is greater than zero, and for an unstable solution, the damping ratio is less than zero. For the work presented here, this process is repeated at several flow conditions presented in Table 3. The damping ratio and the dynamic pressure are interpolated, and at zero damping ratio, the dynamic pressure is considered to be the flutter dynamic pressure. Once this flutter dynamic pressure is identified, the corresponding flutter frequency is determined via an interpolation of the frequencies. In our analysis, we obtained dynamic solutions mainly for the fine grid within the angle of attack range of 0° and 6°. While the first test case for the AePW-3 asks for flutter predictions at only 5° angle of attack, the flutter predictions at other angles of attack provide valuable information on flow physics and shortcomings of uRANS. We repeated the solution process at 1° and 5° only for the coarse grid in the time domain.

The LFD-based mesh adaptation solutions were compared with the LFD solutions at 1° and 5° angles of attack obtained on the coarse and fine grids used in the time-domain computations. This process allows for assessment of efficiency of the mesh-adapted LFD solutions. The flutter dynamic pressure obtained from the time-domain solution over the range of angles of attack is plotted in Figure 3a. The corresponding flutter dynamic pressure obtained from the LFD solution is plotted in Figure 3b. Note that there are multiple points in the LFD with mesh adaptation solutions (shown in red) at higher angles of attack, indicating that for a given mesh adaptation step, the mesh adaptation process (resulting in approximately two million node meshes) did not converge and instead attempted an additional step in the workflow described in the previous section. Figure 4a combines time-domain and LFD flutter predictions and demonstrates a significant departure in computed flutter dynamic pressure past 3° angle of attack for both methods. It is important to remember that in the LFD method flow dynamics is linearized about the mean flow; however, the stability of the BSCW wing at Mach 0.8 and above 3° angle of attack appears to be driven by nonlinear unsteady flow physics. In the experiment, the flutter onset is due to freestream turbulence or a shock buffet. With that, the size of a computational excitation or a 'kick' in the time-domain solution may determine flutter condition. Some preliminary analysis considering different kick magnitude are discussed later in this paper, but further studies are required. Figure 4b is a combined plot of all computed flutter frequencies.

Figure 5 shows the damping values computed at all time-domain flow conditions used in this analysis. The dynamic pressure corresponding to the 'zero' damping-value crossings corresponds to the flutter dynamic pressure shown in Figure 4a. There is a substantial slope shift in the damping curves, where past 3° angle of attack, the magnitude of the

slope changes from large negative to small negative values. The 3° angle of attack is also a location of a departure in flutter dynamic pressure between the time-domain and LFD method attributed to the separated flow behind the shock.

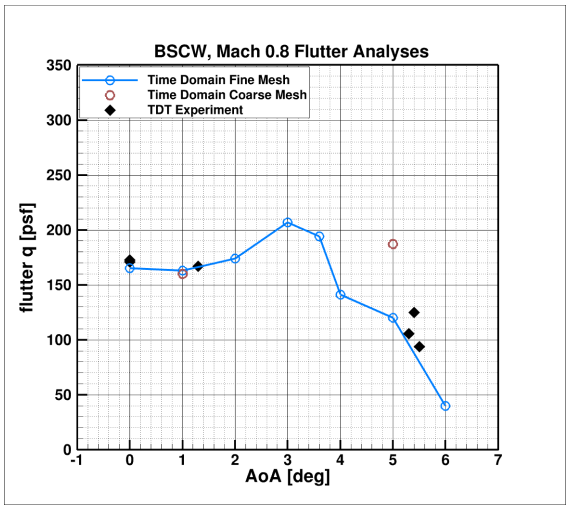

(a) Flutter q: Time Domain.

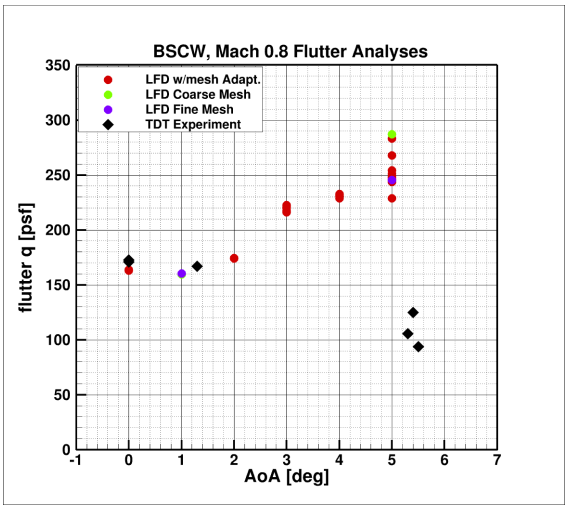

(b) Flutter q: LFD.

Figure 3. Case #1: Flutter Dynamic Pressure in Time and Frequency Domains as Function of Angle of Attack, Mach 0.8.

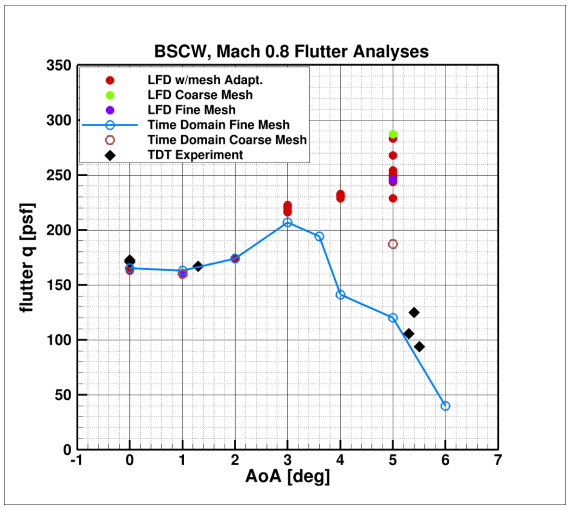

(a) Flutter q: Time Domain and LFD (combined).

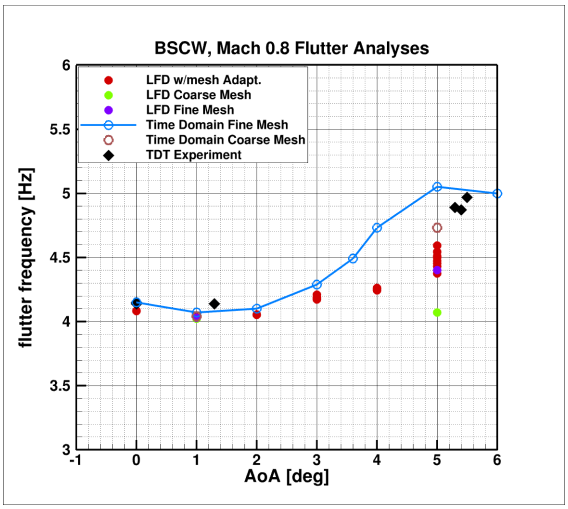

(b) Flutter q and Flutter Frequency: Time Domain and LFD (combined).

Figure 4. Case #1: Flutter Dynamic Pressure and Frequency in Time and Frequency Domains as Function of Angle of Attack, Mach 0.8 (combined plots).

In the previous analysis for AePW-2,[7] it was shown that the proper selection of both the time-step size and number of subiterations in the dual-time stepping scheme is very important in flutter boundary prediction. An application of a temporal error (TE) control parameter to provide a residual-cutoff region for the solution to stop at the subiteration level and to proceed to the next physical time step was also discussed. Based on those results, for the current analysis the dimensional time-step size was set to 0.0002 seconds with a maximum of 50 subiterations, and with a TE parameter set to 0.1 (10%). In addition, a traditional Predictor-Corrector (P-C) scheme was used for the modal solver temporal integration.

As mentioned in Section IIIC, a typical flutter calculation in FUN3D requires an initial excitation 'kick' at the start of the dynamic aeroelastic simulation. This kick can be applied in the form of either (generalized) velocity or force. The magnitude of the kick is somewhat arbitrary; however, it cannot be so large that it causes large grid deformation and possible solution failure. A large kick in the pitch degree of freedom may also change the aerodynamic state of

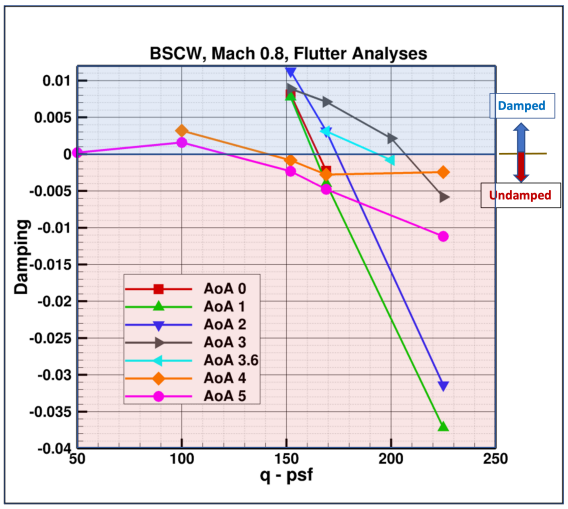

Figure 5. Case #1: Points Used to Determine Flutter Dynamic Pressure, Mach 0.8.

the flow, leading to incorrect flutter prediction for systems assumed to be subject to small perturbations in free stream conditions. On the other hand, a kick that is too small will result in the solution taking a very long time to develop. However, in general, an initial excitation kick might not be required to obtain a flutter solution. It was shown in Reference 7 that the magnitude of the kick did not affect flutter dynamic pressure prediction for a flow condition with an attached flow.

In this analysis, the magnitude of the initial kick was considered to reconcile the difference in flutter prediction between the time-domain and LFD methods and to build on conclusions in Reference 7. As explained in Section IIID, the LFD method assumes infinitesimal oscillatory perturbations. The natural question to ask then is what happens when the magnitude of the kick at the start of the time-domain dynamic solution is reduced from a baseline value K1, to a smaller value K2 (in this case, reduced by an order of magnitude). The results are presented in Table 4 for two dynamic pressure values, 169 psf and 225 psf. As expected, for a baseline kick (K1), the damping value decreases with the increasing dynamic pressure q. This means that with the increasing q, computed wing response becomes more unstable. At the given value of q, the damping increases when the kick magnitude decreases. This in turn means that the wing response changed from unstable to stable. These results suggest that the magnitude of kick does have a significant effect on the computed wing response in a time domain solution, and that the computed wing response with a small excitation kick might approach flutter-q value obtained from the LFD solution. However, further studies are needed to understand the effect of the initial kick on the computed wing response in a presence of a separated flow.

Table 4. Initial Excitation 'Kick' Effect on Damping, Mach 0.8, $\alpha = 5^\circ$, Time-Domain Analysis.

	q = 169 psf	q = 225 psf
K1	- 0.00438	- 0.00961
K2 = 0.1 x K1	0.00231	- 0.002187

V. AePW-3 Test Case #2

The AePW-3 test Case #2 is an optional workshop case that is an extension of a case from AePW-2. As shown previously in Table 1, AePW-2 Case #3a, assessed the rigid-steady versus rigid-unsteady flow calculations in the presence of a shock-induced separated flow, which dominates the upper surface and the aft portion of the lower surface of the BSCW model at Mach 0.85, 5° angle of attack. The flutter prediction presented in Section IV shows the flutter dynamic pressure at Mach 0.8 and 5° angle of attack to be approximately 120 psf. As shown in Table 5, the OTT experimental database consists of several points where the wing (unforced) was kept at fixed angles of attack at several Mach numbers and dynamic pressures, with the unsteady pressure measured at 60% wing span. One of these experimental points consists of data collected at Mach 0.8 with a dynamic pressure of 100 psf (near the flutter q, highlighted in 'red', and corresponding to conditions in 'red' in Table 2) and 5° angle of attack. This section describes the preliminary unsteady flow FUN3D results produced for this case. Computational results are compared with the available experimental pressure data. Future analysis will address the shock-buffet environment.

Table 5. OTT Unforced Wing Experimental Database, A = [0°, 1°, 3°, 5°], B = [-1°, 0°, 1°, 3°, 5°], C = [-1°, 0°, 1°, 2° 3°, 5°].

Q (psf) / Mach	0.5	0.6	0.7	0.8	0.85	0.87
100	B	B	A	C		B
170	B	B	B	B		B
200				B	B	

In this study, the FUN3D flow solver (unsteady-flow analysis) is linked with the Pointwise®[30] mesh generation software to adapt the mesh. Here, an isotropic mesh refinement is accomplished by creating point sources at existing mesh nodes, with spacing based on the interpolation error of Mach number. This error is computed by looping through each node in the mesh and comparing the Mach number at that node to a linear least squares interpolation from all nodes in cells containing the node under consideration. For unsteady adaptation, flow states for a series of time steps are examined, and the error from each is accumulated to provide a refinement field that covers all areas containing error. After a new mesh is generated, the existing flow solution is interpolated to the new mesh and the calculation is repeated until mesh convergence is reached. There are two ways to reach a converged adaption state: 1) all error is below the specified cut off for which the mesh is not refined; 2) all nodes, which have error, are already at the minimum spacing requested in the input. The resulting mesh for both the surface and the plane of symmetry is presented in Figure 6. On the flow solver side, the Delayed Detached Eddy Simulation (DDES)[31] method was used to obtain solutions. The time-step size in the DDES simulation with mesh adaptation is based on the smallest target grid spacing and is set to provide a Courant-Friedrichs-Lewy (CFL), ≤ 1.

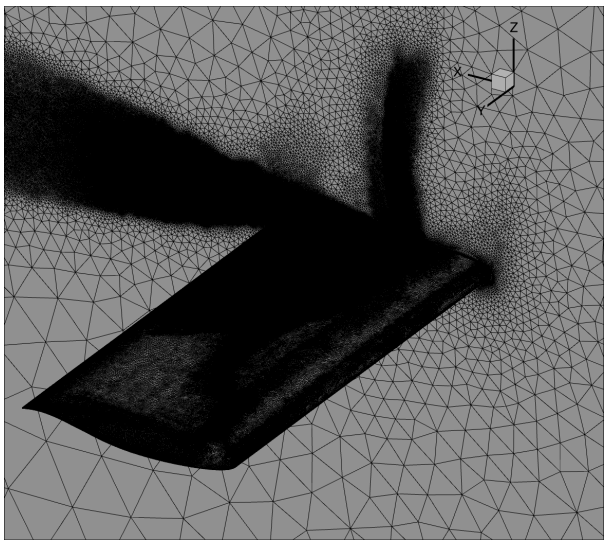

Figure 6. Adapted Mesh, $\sim$ 31 Million Nodes, FUN3D/Pointwise Workflow.

Results presented here are from the fourth mesh adaptation step, where the number of nodes in the mesh reached approximately 31 million. Figure 7a shows the upper wing surface with computed pressure and Mach number on the plane of symmetry (located at the root of the wing) at one discrete point in time during the unsteady flow simulation. The figure also shows eight-span locations labeled 'S1' through 'S8'. The fifth span location, S5, corresponds to 60% wing span, where the experimental pressure data were measured. Locations of experimental pressure sensors on the top of the wing are marked by 22 small aqua-color squares. Figure 7b shows the mean, minimum, and maximum values of pressure coefficient, c_p. Pressure data from the pressure sensors at locations 10-14 and 20 identified in Figure 7a were used to compare experimental and computational pressure data. Figures 8a and 8b show the time history of the pressure coefficients obtained from the experiment and computations, respectively. The results show that the shock at this flow condition is located downstream of sensor 11 in the experiment and downstream of sensor 10 in the computation. Pressure magnitudes are approximately the same in experiment and computations at sensor locations 10 and 20, but they are different at locations 12 through 14. The numerical results show that the shock location at the 60% span location is affected by the shock propagating from the leading edge of the wing tip. This in turn establishes a nonuniform spanwise flow distribution, where up to span station S4, the flow appears to be separated. To further evaluate flow in that region, pressure coefficients at spanwise location S3 and corresponding to pressure sensors 10-14 and 20 were extracted from the FUN3D solution and are plotted in Figure 9. Comparison of pressure at sensor location 20 in Figure 8b and in Figure 9 shows significantly more pressure fluctuations at span station S3 than S5. However, further mesh adaptation steps and longer time-record lengths are needed to assess the goodness of a predicted shock location and of the flow state behind the shock across the wing span. So far, computationally, only approximately of 0.25 seconds of pressure data were obtained. Because of that, the FFT of only the experimentally-obtained pressure coefficient data are presented in this paper in Figure 10a. A longer computational time record of pressure is needed to properly compare frequency content with the experimental data. However, initial results (not presented) suggest a 20 Hz fundamental frequency in the computational pressure time history at sensor location 10 through 14. This is encouraging and similar to the experimental data.

As noted before and shown in Figure 7a, the computed spanwise pressure distribution is nonuniform. The time history of sectional lift coefficients were computed at eight span location and are compared with the time history of the global lift coefficient in Figure 10b. Future work will present computed FFT of each sectional lift coefficient together with an FFT of global lift coefficient.

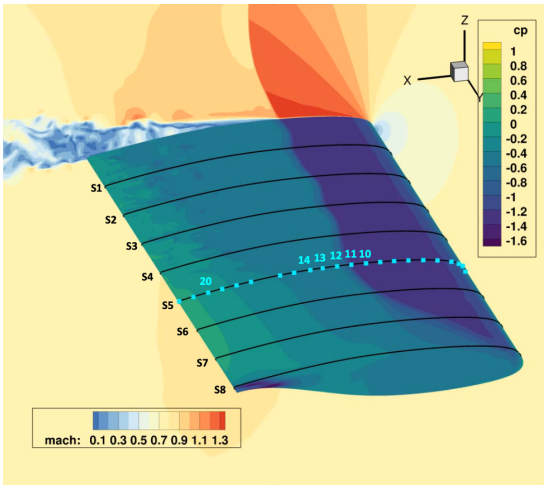

(a) Surface Pressure and Symmetry Plane Mach Number.

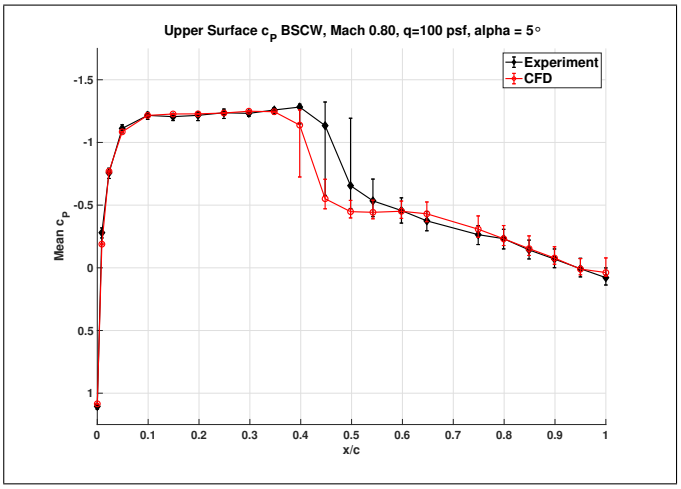

(b) Mean Pressure Coefficients and Min/Max Bounds from Experiment and FUN3D at 60% (S5) Wing Span

Figure 7. BSCW Flow and Experimental Data at Mach 0.8, angle of attack 5°, q = 100 psf.

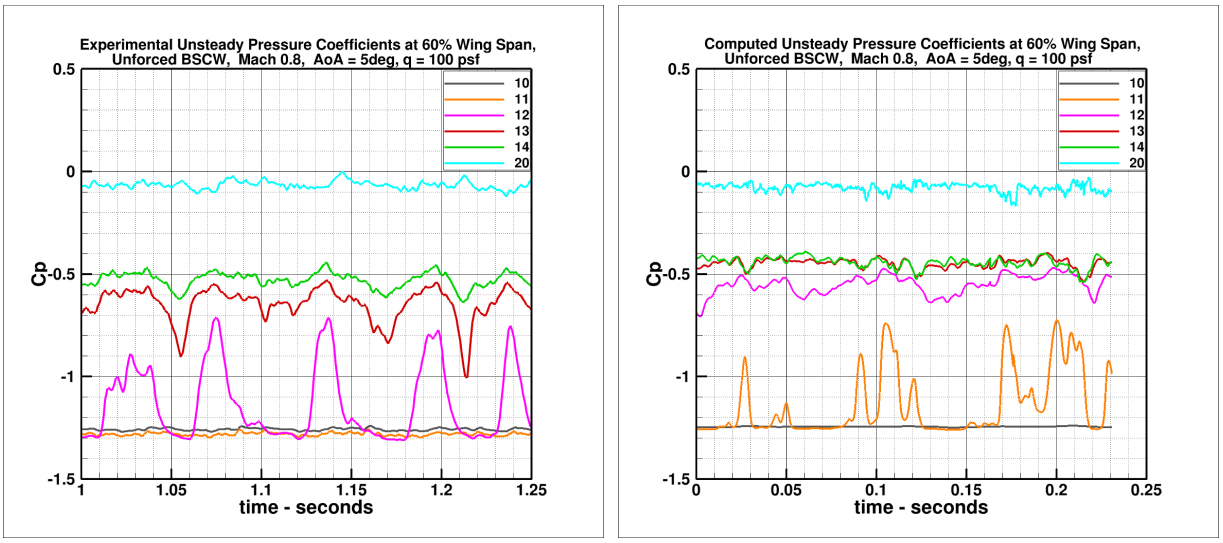

(a) Experiment. (b) CFD.

Figure 8. Experimental and Computational Pressure at S5 Span and Sensor Locations 10-14 and 20, BSCW Case #2, Mach 0.8, angle of attack 5°, q = 100 psf.

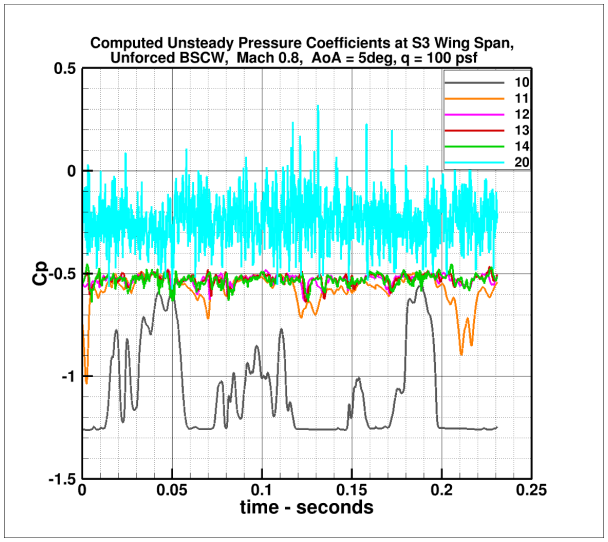

Figure 9. Computational Pressure at S3 Span and Sensor Location 10-14 and 20, BSCW Case #2, Mach 0.8, angle of attack 5°, q = 100 psf.

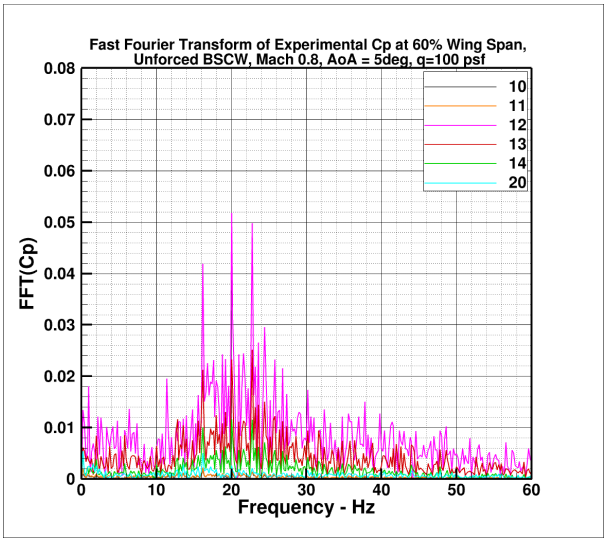

(a) FFT of Experimental Pressure at S5 Span and Sensor Location 10-14 and 20

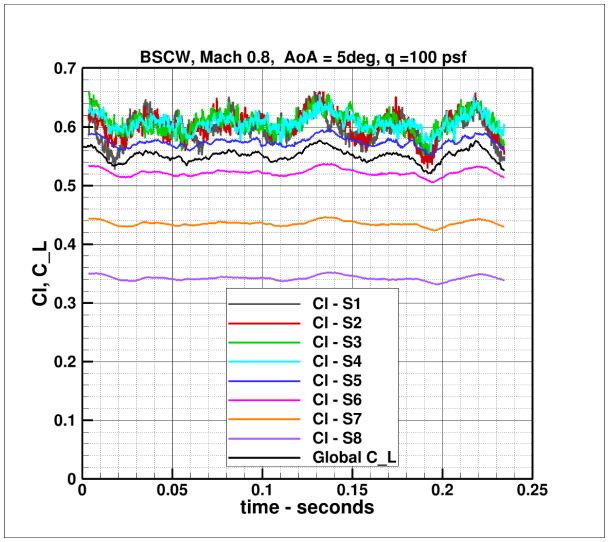

(b) Sectional vs. Global Lift Coefficients.

Figure 10. FFT and Sectional Lift Coefficients, BSCW Case #2, Mach 0.8, angle of attack 5°, q = 100 psf.

VI. Concluding Remarks

Unsteady Reynolds-averaged Navier-Stokes analyses were performed as part of the AePW-3 workshop using the NASA Langley FUN3D software. Analyses were performed for BSCW flutter configurations considered for the workshop. These preliminary analyses show a need for higher fidelity methods to compute flutter and shock-and-boundary layer interaction. The computationally-obtained flutter dynamic pressure at Mach 0.8 and 5° angle of attack is approximately 120 psf. Only a preliminary assessment of the unforced-wing unsteady flow computations using DDES was made. Results are encouraging, but longer computational time histories are needed to evaluate frequency content in the unsteady flow and the corresponding shock-buffet existence.

VII. Acknowledgments

Aeroelastic workshop series is supported by the Transformational Tools and Technologies (TTT) project at NASA Langley. Computational resources for this work are provided by NASA Supercomputer Center (NAS) and by the NASA Langley K cluster.

References

[1]Heeg, J., Wieseman, C. D., and Chwalowski, P., "Data Comparisons and Summary of the Second Aeroelastic Prediction Workshop," AIAA Paper 2016-3121, 2016.

[2]Dansberry, B. E., Durham, M. H., Bennett, R. M., Turnock, D. L., Silva, W. A., and Rivera, J. A., "Physical Properties of the Benchmark Models Program Supercritical Wing," NASA Technical Memorandum 4457, 1993.

[3]Dansberry, B. E., Durham, M. H., Bennett, Rivera, J. A., Silva, W. A., and Wieseaman, C. D., "Experimental Unsteady Pressures at Flutter on the Supercritical Wing Benchmark Model." AIAA Paper 1993-1592-CP, 1993.

[4]Piatak, D. J. and Cleckner, C. S., "A New Forced Oscillation Capability for the Transonic Dynamics Tunnel," AIAA Paper 2002-0171, Jan. 2002.

[5]Heeg, J. and Piatak, D. J., "Experimental data from the Benchmark SuperCritical Wing wind tunnel test on an oscillating turntable," AIAA Paper 2013-1802, April 2013.

[6]Chwalowski, P. and Heeg, J., "FUN3D Analyses in Support of the Second Aeroelastic Prediction Workshop," AIAA Paper 2016-3122, June 2016.

[7]Chwalowski, P., Heeg, J., and Biedron, R., "Numerical Investigations of the Benchmark Supercritical Wing in Transonic Flow," AIAA Paper 2017-0190, Jan. 2017.

[8]http://fun3d.larc.nasa.gov/papers/FUN3D_Manual-13.7.pdf, *NASA/TM-2020-5010139*.

[9]Jacobson, K., Stanford, B., Wood, S., and Anderson, W., "Flutter Analysis with Stabilized Finite Elements based on the Linearized Frequency-domain Approach," AIAA Paper 2020-0403, Jan. 2020.

[10]Schuster, D. M., "Aerodynamic Measurements on a Large Splitter Plate for the NASA Langley Transonic Dynamics Tunnel," NASA TM 2001-210828, March 2001.

[11]Pirzadeh, S. Z., "Advanced Unstructured Grid Generation for Complex Aerodynamic Applications," AIAA Paper 2008–7178, Aug. 2008.

[12]Samareh, J. A., "Unstructured Grids on NURBS Surfaces," AIAA Paper 1993–3454.

[13]http://nescacademy.nasa.gov/workshops/AePW2/public/.

[14]http://turbmodels.larc.nasa.gov/spalart.html.

[15]Spalart, P. R. and Allmaras, S. R., "A One-Equation Turbulence Model for Aerodynamic Flows," *La Recherche Aerospatiale*, No. 1, 1994, pp 5–21.

[16]Venkatakrishnan, V., "Convergence to Steady State Solutions of the Euler Equations on Unstructured Grids with Limiter," *Journal of Computational Physics*, Vol. 118, No. 1, April 1995, pages 120-130.

[17]Roe, P. L., "Approximate Riemann Solvers, Parameter Vectors, and Difference Schemes," *Journal of Computational Physics*, Vol. 43, No. 2, October 1981, pages 357-372.

[18]Biedron, R. T. and Thomas, J. L., "Recent Enhancements to the FUN3D Flow Solver for Moving-Mesh Applications," AIAA Paper 2009-1360, Jan. 2009.

[19]Biedron, R. T. and Lee-Rausch, E. M., "Rotor Airloads Prediction Using Unstructured Meshes and Loose CFD/CSD Coupling," AIAA Paper 2008-7341, 2008.

[20]Batina, J. T., Seidel, D. A., Bland, S. R., and Bennet, R. M., "Unsteady Transonic Flow Calculations for Realistic Aircraft Configurations," AIAA Paper 1987-0850, 1987.

[21]Bartels, R. E., Rumsey, C. L., and Biedron, R. T., "CFL3D Version 6.4 - General Usage and Aeroelastic Analysis," NASA TM 2006-214301, March 2006.

[22]MSC Software, Santa Ana, CA, *MSC Nastran*, 2008, http://www.mscsoftware.com/products/msc_nastran.cfm.

[23]Samareh, J. A., "Discrete Data Transfer Technique for Fluid-Structure Interaction," AIAA Paper 2007–4309, June 2007.

[24]Heeg, J., Chwalowski, P., Schuster, D. M., Raveh, D., Jirasek, A., and Dalenbring, M., "Plans and Example Results for the 2nd AIAA Aeroelastic Prediction Workshop," AIAA Paper 2015-0437, Jan. 2015.

[25]Vatsa, V. N., Carpenter, M. H., and Lockard, D. P., "Re-evaluation of an Optimized Second Order Backward Difference (BDF2OPT) Scheme for Unsteady Flow Applications," AIAA Paper 2010-0122, Jan. 2010.

[26]Anderson, W., Newman, J., and Karman, S., "Stabilized Finite Elements," *Journal of Aircraft*, Vol. 55, No. 2, 2017, pages 696-714.

[27]Jacobson, K., Stanford, B., Kiviaho, J., Park, M., and Chwalowski, P., "Multiscale Mesh Adaptation for Transonic Aeroelastic Flutter Problems," AIAA Paper 2021-2700, Aug. 2021.

[28]Alauzet, F., George, P., Mohammadi, B., Frey, P., and Borouchaki, H., "Transient Fixed Point-Based Unstructured Mesh Adaptation," *International Journal for Numerical Methods in Fluids*, Vol. 43, No. 6-7, 2003, pages 729-745.

[29]Kiviaho, J., Jacobson, K., and Kennedy, G., "Flutter Boundary Identification from Time-Domain Simulations Using the Matrix Pencil Method," Tech. rep., Vol. 57, No. 8, August 2019, pages 3639-3645.

[30]*Pointwise, V18.4R2*, https://https://www.pointwise.com.

[31]Vatsa, V. N. and Lockard, D. P., "Assessment of Hybrid RANS/LES Turbulence Models for Aeroacoustics Applications," AIAA Paper 2010-4001, 2010.